# First-principles study of Ti-doped sapphire. I. Formation and optical transition properties of titanium pairs

Weiguo Jing [1,2,3] Mingzhe Liu,[1,4] Jun Wen,[5] Lixin Ning,[6] Min Yin,[4] and Chang-Kui Duan [1,2,3,*]

[1]*Hefei National Laboratory for Physical Sciences at the Microscale and Department of Physics, University of Science and Technology of China, Hefei 230026, China*

[2]*CAS Key Laboratory of Microscale Magnetic Resonance, University of Science and Technology of China, Hefei 230026, China*

[3]*CAS Center for Excellence in Quantum Information and Quantum Physics, University of Science and Technology of China, Hefei 230026, China*

[4]*CAS Key Laboratory of Strongly-Coupled Quantum Matter Physics, University of Science and Technology of China, Hefei 230026, China*

[5]*School of Electronic Engineering and Intelligent Manufacturing, Anqing Normal University, Anqing 246133, China*

[6]*Anhui Province Key Laboratory of Optoelectric Materials Science and Technology, Key Laboratory of Functional Molecular Solids, Ministry of Education, Anhui Normal University, Wuhu, Anhui 241000, China*

Titanium sapphire is one of the most important laser crystals suitable for widely tunable and ultrashort pulsed lasers with high gain and high power outputs, but its performance is limited by the residual infrared absorption at the operation wavelength region of the laser. Although studies have been made over decades in improving the laser performance and the solutions to eliminate this residual absorption, there still remain some controversies for the binding tendency and charge-transfer transition energy of Ti related pairs, which is supposed to be the culprit of this residual absorption. In this paper, we clarify that previously predicted strong binding tendencies in $Ti^{3+}$-$Ti^{3+}$ and $Ti^{3+}$-$Ti^{4+}$ pairs should be artificial and are blamed on the intrinsic delocalization error in general approximate density functionals. We show that such errors can be eliminated by Hubbard $U$ corrected generalized-gradient-approximation method with $4 \leqslant U \leqslant 5\,\mathrm{eV}$ or hybrid density functionals such like HSE06 and PBE0, which approximately satisfy the generalized Koopmans' condition. Our calculations reveal that the equilibrium geometry and electronic structure of $Ti^{3+}$-$Ti^{4+}$ pairs can be $Ti^{3+}$-$Ti^{4+}$-type or $Ti^{3.5+}$-$Ti^{3.5+}$-type configurations with very small energy differences ($\lesssim 0.1\,\mathrm{eV}$), and both of them have residual infrared absorption, which are predicted to be about three orders of magnitude stronger in oscillator strength per defect than the pump absorption of $Ti^{3+}$ dopants. Regarding $Ti^{3+}$-$Ti^{3+}$ pairs, it is shown that they do not contribute to the residual infrared absorption in the wavelength range of laser operation, but their charge-transfer transitions can explain the residual UV band at 270 nm and $E$ band at 400 nm in the absorption spectra of $Ti:Al_2O_3$ crystals. Furthermore, the charge-transfer transition energies and Stokes shift of $Ti^{4+}$ and ionization energies for $Ti^{3+}$ are also well interpreted by our calculations. The calculation method developed together with the predicted optical properties forms the basis for exploration on eliminating the residual infrared absorption in titanium sapphire.

## I. INTRODUCTION

Titanium sapphire ($Ti:Al_2O_3$) is one of the most important laser crystals and has broad applications in scientific and medical research areas [1–6]. There is a so-called residual infrared (IR) absorption [7] whose broad absorption band is centered near 800 nm, in exactly the lasing wavelength range, and extremely limits the improvement of the laser performance [5]. According to the phenomenological model, Aggarwal *et al.* attributed the residual IR absorption largely to the absorption of a $Ti^{3+}$-$Ti^{4+}$ pair [7]. This illustration has been supported by a subsequent experiment of electron spin resonance and optical measurements carried out by Yamaga *et al.* [8], who further indicated that there is a charge compensating aluminium vacancy $V_{Al}^{3-}$ at a neighboring site of a $Ti^{3+}$-$Ti^{4+}$ cluster. Such a

$Ti^{3+}$-$Ti^{4+}$ pair model has been the most accepted explanation for the residual IR absorption [9].

The first-principles calculation based on density functional theory (DFT) [10–13], which has made many great achievements in simulations throughout physical and material sciences [14,15], has also been applied to explore this residual IR absorption issue [16–18]. These works show that the binding energy $E_B$, i.e., the energy released in forming a $Ti^{3+}$-$Ti^{3+}$ pair is at around 1.3 eV, and, more recently, the $E_B$ of $Ti^{3+}$-$Ti^{4+}$ pair has been calculated as $\sim$0.7 eV [17,18]. This is at odds with Ref. [19], where the binding energy of $Ti^{3+}$-$Ti^{4+}$ pair was estimated to be essentially zero.

Moreover, the concentrations $c_{Ti^{3+}-Ti^{3+}}$ of the $Ti^{3+}$-$Ti^{3+}$ pair and $c_{Ti^{3+}}$ of $Ti^{3+}$ ion (normalized to the concentration of the aluminium site in the host) are related by $c_{Ti^{3+}-Ti^{3+}} = A \exp(E_B/kT) c_{Ti^{3+}}^2$ under equilibrium distribution of defects, where $A = 1/2$ and $3/2$, correspondingly, for the pairs formed by two Ti ions in the nearest and next-nearest neighbors. The enhancement factor $\exp(E_B/kT)$ equals 1 for the case of

*ckduan@ustc.edu.cn

$E_B = 0$ eV, i.e., no tendency of aggregation of $Ti^{3+}$ dopants, but is about $2 \times 10^3$ for $E_B = 1.3$ eV and $T = 2000$ K, a quite high annealing temperature relative to $Al_2O_3$'s melting point of 2327 K. Such a large factor means that the concentration of the nearest and next-nearest $Ti^{3+}$-$Ti^{3+}$ pairs is comparable with the concentration of $Ti^{3+}$ at the doping level of over 250 ppm (parts per million). However, the photoluminescent properties of $Ti^{3+}$ in a large variety of samples from different sources do not display any apparent changes in peak positions, shapes, and quenching behavior as the doping level changes [9].

To sum up, the clustering tendencies of $Ti^{3+}$-$Ti^{3+}$ and $Ti^{3+}$-$Ti^{4+}$ appear to be controversial and need to be clarified. The contradiction in the binding energy of Ti pairs deteriorates the reliability of DFT calculations in predicting the geometric and electronic properties of aggregated Ti dopants, especially the $Ti^{3+}$-$Ti^{4+}$ pair, not to mention in analyzing and interpreting the charge state and concentration of different defects for the purpose of mitigating the residual IR absorption, which may hamper reliably interpreting the photoluminescence processes and pinpointing the solution to eliminate this residual absorption in experiments.

In this paper, we show that the general DFT functional such as generalized gradient approximation (GGA) fails to satisfy the generalized Koopmans' condition that the total energy for the exact functional of DFT should be a linear function of the fractional occupation numbers [20,21], while DFT $+ U$ with appropriate $U$ and hybrid DFT can approximately fulfill this required condition by tuning the parameters involved. Hence, we determine the $U$ parameter for DFT $+ U$ and obtain the geometric structures and formation energies of various $Ti^{3+}$-$Ti^{3+}$ and $Ti^{3+}$-$Ti^{4+}$ pairs with properly determined charge corrections. We confirm that the high binding tendency is artificial and should be blamed on the intrinsic error of a conventional DFT functional [22]. The DFT $+ U$ results are also compared to the results obtained via hybrid DFT methods that are feasible for small supercells only due to computational costs.

We also study the electronic structure and optical transitions of $Ti^{3+}$-$Ti^{3+}$, $Ti^{3+}$-$Ti^{4+}$, and $Ti^{3+}$ by employing the embedded cluster defects calculations. Based on the energy-level structures and transition rates, we discuss the relevance of these defects to the various absorption bands observed in experiments, especially the residual IR absorption that limits the laser performance.

## II. METHODOLOGY

### A. Computational procedure in VASP

The first-principles calculations based on DFT are performed using the VASP code [23–26], where the plane-wave basis set is adopted to expand the eigenwave function and projector augment wave pseudopotentials are used to describe the interactions of atoms [27,28]. For the exchange-correlation term in DFT, the PBEsol version of the GGA functional whose parameters are specifically optimized for crystal [29,30] and the DFT $+ U$ method is adopted to consider the localization effect of $d$ electron in transition element by applying the $U$ value-related correction in the exchange-correlation func-

tional [31,32]. The $U$ value for $3d$ electrons of Ti, or more precisely the effective $U_{eff} = U - J$ value if another parameter $J$ is not set to 0, varies from 2 to 5 eV in different materials and sometimes is decided semiempirically by choosing the one that predicts consistent results with experiments [30,33–37]. In this paper, we choose $U = 4$ eV for the $3d$ electron of Ti ions in $Ti:Al_2O_3$ by requiring the density functionals to fulfill the generalized Koopmans' condition [20,21], and the details about the determination of $U$ value will be discussed in Sec. III B.

For the structure optimization of a $\alpha$-$Al_2O_3$ primitive cell (space group $R$-$3c$), the original structure comes from the Inorganic Crystal Structure Database with code 26790, and the crystal lattice and atomic positions are fully relaxed by using a $9 \times 9 \times 9$ $k$-point sampling of the Brillouin zone. The supercell method is employed to calculate the binding energy for Ti-related pairs in $Ti:Al_2O_3$ crystal. Supercells of various sizes from 120 atoms to 960 atoms are constructed based on the relaxed primitive cell, and then their sizes and shapes are fixed during the structure relaxation. In addition, the calculations adopt the single $\Gamma$ point in the Brillouin zone for large supercells. The plane-wave cutoff energy is set at 520 eV in the structure optimization of primitive cell and the 120 defect-containing supercells for spectroscopic calculations, while a smaller cutoff energy of 400 eV is used in these defect-related calculations of formation energies as a compromise between the calculation accuracy and computational costs. In all the structure relaxation, the total energy variation is converged to $10^{-3}$ meV/atom and the absolute residual force for each atom is less than 5 meV/Å.

Based on Refs. [38–40], the formation energy of defect or complex $X$ in charge state $q$, as an approximate formation Gibbs free energy at the low temperature and zero pressure limit, can be written as follows:

$$E_f(X^q) = [E_{tot}(X^q) + E_{corr}] - E(bulk) - \sum_i \Delta n_i \mu_i + q E_F. \tag{1}$$

In this expression, $E_{tot}(X^q)$ is the total energy of a supercell containing a $X^q$ defect or complex, and $E(bulk)$ is the total energy of the corresponding pristine supercell. $\Delta n_i$ means the number change of $i$-type atoms between doped structure and the host, i.e., if $\Delta n_i > 0$, $i$-type atoms are added into the supercell when the defect or complex structure is created, and the $\mu_i$ corresponds to the chemical potential of this species which depends on the synthesis condition. The term $E_F \equiv \varepsilon_{VBM} + \Delta\varepsilon_F$ represents the Fermi level, where $\varepsilon_{VBM}$ is the valence-band maximum (VBM) of the host.

The correction $E_{corr}$ comes from the supercell method with periodic boundary conditions in practical DFT calculations [41]. It usually includes two parts, the electrostatic image-charge interaction and the neglect of the average potential difference between doped and pristine supercells [40]. $E_{corr}$ is dependent on the supercell size $L$ and approaches zero as $L \to \infty$. Here, we follow Ref. [42] by using the extrapolation method to obtain $E_f(L \to \infty)$, the formation energy of charged defects or complex in the dilute limit. The equation adopted in the extrapolation is as follows:

$$E_f(L) = E_f(L \to \infty) + \frac{a_1}{L} + \frac{a_3}{L^3}, \tag{2}$$

where $L$ is the length scale of the near cubic supercell so defined that $L^3$ equals the volume of the supercell, and $a_1$ and $a_3$ are coefficients to be determined by fitting the calculated formation energies for a series of supercells of different size $L$. In this paper, the 120, 160, 180, 240, 380, 500, 660, 800, and 960 atoms supercells are used, and the details about the procedures to obtain $E_{corr}$ in Eq. (1) can be found in Supplemental Material Sec. S1 [43].

The binding energy $E_b$ for a complex is calculated as follows:

$$E_b = E_f(AB^{q_1+q_2}) - [E_f(A^{q_1}) + E_f(B^{q_2})], \qquad (3)$$

where $E_f(AB^{q_1+q_2})$, $E_f(A^{q_1})$, and $E_f(B^{q_2})$ are the corrected formation energies for complex $AB^{q_1+q_2}$, and simple defects $A^{q_1}$ and $B^{q_2}$, i.e., extrapolated to the dilute limit ($L \rightarrow \infty$), respectively. It is noted that the binding energy $E_b$ defined here is just the energy to form an isolated complex defect from its composition defects. It differs by a minus sign from the $E_B$ mentioned in Sec. I.

To test the influence of using the $\Gamma$ point integration in our results, the 120, 160, 180, 240, and 380 atoms supercells—those are smaller supercells in our extrapolation method—have been built to obtain the total energies of $Ti^{3+}$, $Ti^{4+}$, $Ti^{3+}$-$Ti^{3+}$, $Ti^{3+}$-$Ti^{4+}$, and $Ti^{4+}$-$Ti^{4+}$. The k-point mesh grids are set as $2 \times 3 \times 4$, $3 \times 3 \times 3$, $3 \times 4 \times 4$, $3 \times 4 \times 5$ and $5 \times 5 \times 5$ for our smallest supercell, 120 atoms included, while in the other supercells, calculations are obtained by integrating over $2 \times 3 \times 4$, $3 \times 3 \times 3$ grids of $k$ points. Our calculation shows that the difference between doped supercell and corresponding pristine bulk depends on $k$-points mesh grids weakly (see Supplemental Material Sec. S2 [43] for detailed comparison), and the single $\Gamma$ point integration will only introduce an error of $\sim 0.01$ eV or less for the formation energy of defect in the isolated limit. In addition, thanks to the error cancellation in Eq. (3), these kinds of errors have less influence on binding energies.

We have also checked the local structures of each defect in supercells of different sizes and find that they are all fully relaxed. For example, the bond lengths of $Ti^{3+}$-$Ti^{4+}$ in the 960-atom supercell differ from those in 800-atom supercell by $\lesssim 0.1\%$, and from those in 120-atom supercell by $\lesssim 0.3\%$ (see Fig. S2 in Supplemental Material Sec. S3 for details [43]).

### B. Energy levels and transition rate calculations based on the embedded cluster model

The energy-level structures and the transition oscillation strengths for Ti pairs are calculated via the embedded cluster model with the MOLCAS program [51], where the geometric structure of the cluster containing the Ti pairs is constructed from the supercells relaxed via VASP as follows.

To construct the base cluster for MOLCAS, the 960-atom undoped supercell whose atoms are fully relaxed is adopted as the pristine bulk, and then two Al ions near the center of the supercell are substituted with two Ti ions to construct the raw doped supercell, which is then fully relaxed. During the relaxation of the doped supercell, the size and shape of this supercell is fixed so it can be embedded seamlessly in the infinity crystal lattice of $Al_2O_3$ bulk that has been constructed

by the translation of the relaxed 960-atom undoped supercell. Next, the midpoint of the line segment connecting the two Ti ions is taken as the origin and those atoms within the sphere of a radius 40 Å or larger are included in the base cluster.

Owing to computational constraints, the base cluster structure is further divided into three parts, i.e., a small center cluster, a surrounding sphere and a peripheral shell, which are treated differently. The center cluster and surrounding sphere compose the core cluster of a radius about 10 Å with the above-defined origin. The core clusters are represented by the embedding *ab initio* model potentials [52]. Specifically, the valence electrons in center cluster which contains the two Ti ions and their nearest-neighbor O atoms, are handled by adopting the relativistic effective core potential ([Mg]-core) for Ti with a $(9s6p6d)/[3s3p4d]$ Gaussian valence basis set and the [He]-core effective core potential for O with a $(5s6p1d)/[2s4p1d]$ Gaussian valence basis set according to Ref. [53]. For those Al and O atoms in the surrounding sphere, all electrons are frozen.

The rest part of the base cluster, i.e., the peripheral shell are treated as a large collection of effective point charges, and the thickness of this shell is well regulated (about 40 Å or larger) to let the difference of the static Coulomb potential at the two Ti atoms, which is contributed by all the effective point charges in the peripheral shell, equal to the one obtained for the peripheral shell with infinite radius.

The multiconfigurational self-consistent field (SCF) calculation is performed to obtain the energy levels as well as corresponding wave functions of the clusters by using the complete active space SCF (CASSCF) method [54]. For the $Ti^{3+}$-$Ti^{4+}$ pair, $(Ti_2O_9)^{11-}$ for *nearest* and $(Ti_2O_{10})^{13-}$ for *next* configurations are constructed as the embedded clusters. The energy levels and wave functions are obtained by minimizing the average energy of the lowest ten states, which is generated by occupying the single unpaired electron on one of these ten molecular orbitals whose main characters are $3d$ of Ti ions. In the $Ti^{3+}$-$Ti^{3+}$ pair, embedded clusters are $(Ti_2O_9)^{12-}$ for *nearest* and $(Ti_2O_{10})^{14-}$ for *next* configurations, and both $S = 0$ (antiferromagnetic) and $S = 1$ (ferromagnetic) geometric structures are considered. For each cluster, the active space composes the 190 basis states by the distribution of two electrons in ten molecular orbitals of the Ti-$3d$ character. Finally, the energy levels and wave functions are obtained by minimizing the average energy of 45 spin parallel states and 55 spin antiparallel states separately.

The dynamic electron correlation effect for $3d$ of Ti and $2p$ of O atoms has been included by using the second-order many-body perturbation theory (termed CASPT2) with CASSCF wave functions [55]. The restricted active space state interaction program [56] is adopted to calculate the oscillation strength for electric dipole optical transitions. It is noted that the oscillator strengths are calculated for a cluster, which is in essence a molecular in vacuum, so the effect of the dielectric media on the local electric field and speed of light has not been taken into account. Such effect can usually be taken into account approximately by multiplying a refractive-index $n$ related correction factor as $\chi = (n^2 + 2)^2/9n$, namely, local-field correction [57]. For $Al_2O_3$, $n = 1.760$ (at 800 nm) and 1.775 (at 490 nm), so $\chi \approx 1.65$.

TABLE I. The lattice parameters in our calculation versus results in literature

| Parameter | This work (PBEsol) | Calculation (PBEsol) [58] | Expt. [59] |
|---|---|---|---|
| $a$(Å) | 4.77 | 4.75 | 4.76 |
| $c$(Å) | 13.01 | 12.96 | 12.99 |

## III. RESULTS AND DISCUSSIONS

### A. The basic structure of Al₂O₃ bulk

The primitive cell of $\alpha$-$Al_2O_3$ (space group $R$-$3c$, No. 167) contains ten atoms, i.e., two chemical formula $Al_2O_3$ units, while the conventional hexagonal unit cell, which consists of six formula units, is more frequently used in calculations and experiments. Although the primitive cell is employed as the basic unit in our work to construct the supercells, lattice parameters of primitive cell have been transformed to hexagonal result for better comparing with previous DFT calculations and experiments in Table I.

The aluminum and oxygen ions in $\alpha$-$Al_2O_3$ occupy one $12c$ and $18e$ Wyckoff positions, respectively. Each Al ion locates at the center of a distorted octahedral geometry which is composed of six surrounding oxygen atoms, where three coplanar oxygen atoms in the octahedral geometry are closer to the Al center than the other three. Therefore, the Al-O distances are divided into two groups, 1.86 Å and 1.97 Å, very close to previous calculations [60,61] and the experiment [62]. In addition, each Al ion has one nearest Al site along the threefold axis of the conventional unit cell and three equivalent next-nearest Al sites. These octahedral units are connected by face-sharing and edge-sharing modes as shown in Fig. 1.

### B. The determination of $U$ parameter in GGA + $U$ method

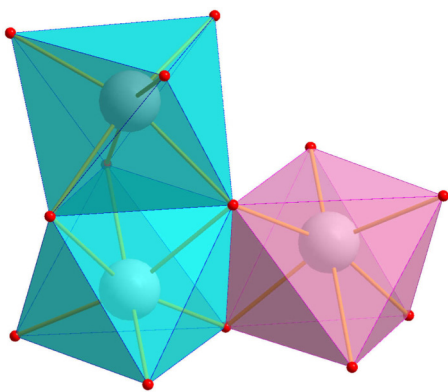The envied exact density functional satisfies the generalized Koopmans' condition that the total energy of the



FIG. 1. Three octahedral units in $\alpha$-$Al_2O_3$ are drawn to show the local environment of Ti ions. The white balls are Al atoms and red balls are oxygen atoms. Two cyan octahedral units are connected by the face-sharing mode where these two units share three oxygen atoms, and the cyan and pink octahedrons are connected in edge-sharing mode by sharing two oxygen atoms.
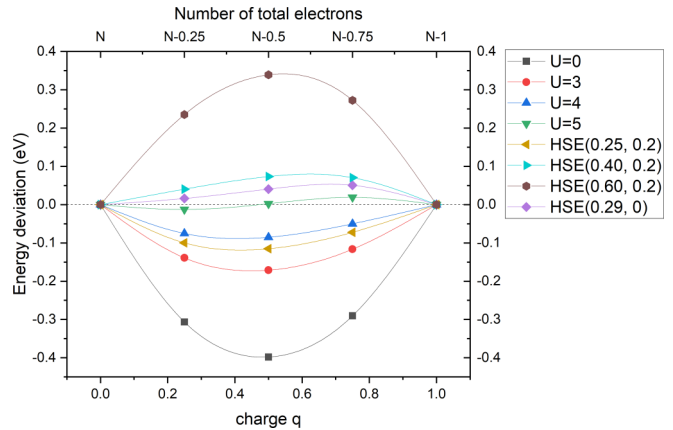


FIG. 2. The deviations of total energy function $E_{tot}(Ti^{3+q})$ between exact functional and GGA + $U$ results, where $U = 0, 3, 4, 5$ (in units of eV). Several HDFT methods in HSE($\alpha, \mu$) functional are also used as references, where $\alpha$ is the HF mixing parameter and $\mu$ is the screen parameter. $N - q$ is the total number of electrons.

system is a piecewise linear function of electron numbers, i.e., the dependence of total energy on fractional interpolation between integer occupation is linear [20,21,63]. This is a natural requirement in the open atomic system to describe the intermediate situation, a system with noninteger electrons, which represents the statistical mixture of systems with integer electrons [63,64]. However, in a practical DFT approximation such as GGA, the total energy is usually a parabolic convex function of the number of electrons, which is related to the deficiency in the approximation of the exchange-correlation term. This convex behavior in the DFT functional tends to cause an artificial delocalization for electrons, especially for the localized $d$ or $f$ electrons, and an incorrect description of the interaction between electrons [22,65]. In the DFT + $U$ method, this delocalization error can usually be eliminated by mathematically adding a $U$ parameterized concave term in the exchange-correlation functional for error cancellation or in a more physical explanation by considering the local effect of electrons in Hubbard model [20,66]. Thus, an improved description of the system can be obtained in practical DFT calculations by choosing an appropriate $U$ value.

Since Ti contains an open $3d$ shell, the locality of $3d$ electrons and their on-site interactions need to be treated properly. The $U$ value in GGA + $U$ is determined by considering the simple case of an $Al^{3+}$ ion substituted by a $Ti^{3+}$ ion whose total energy is supposed to vary linearly with the extra charge $q$ on the defect from 0 to 1. In a $Al_2O_3$ supercell of 120 atoms, the $Ti^{3+}$ defect is fully relaxed to obtain the optimized ground configuration. Then we fix this configuration but change the electron number, i.e., a positive fractional charge exists on the defect $Ti^{3+q}$ [$q \in (0, 1)$]. The total energy is calculated as a function of the fractional charge for a series of $U$ values, and we display their total energy deviations between our calculation results and linear functions of total energy as a requirement of the exact functional (Fig. 2). It is noted that the charge correction for the total energy has been taken into account in the calculation, and we find that the influence of the Hubbard $U$ correction to the charge correction result can

be neglected (see Supplemental Material Fig. S1 and related discussion in Sec. S1 [43] for details).

In addition, it is believed that the hybrid density functional theory (HDFT) can improve the description of total energy (over the GGA method) in fulfilling the general Koopmans' condition by properly mixing both convex and concave components in the functional [22,35]. We therefore choose one of the most popular HDFT functionals, which was developed by Heyd, Scuseria and Ernzerhof (HSE) [67] as a reference to the GGA + $U$ method in Fig. 2. The HSE functional contains two parameters: the HF mixing parameter $\alpha$ and the screen parameter $\mu$. HSE06 ($\alpha = 0.25$, $\mu = 0.2$) [68] is one of the most widely used functionals, while HSE($\alpha = 0.40$, $\mu = 0.2$) gives a more appropriate band gap as 9.22 eV for $Al_2O_3$, which is close to the 9.1 eV measured at low temperature [69] and previous calculation 9.1 eV with GW method [70], and HSE($\alpha = 0.60$, $\mu = 0.2$) is also included to show the tendency of the energy function as $\alpha$ increases. Apart from HSE06, PBE0-type functional (denoted as PBE0), with $\mu = 0$ and $\alpha = 0.29$ determined by following Ref. [71], is also considered in our calculations and the band gap obtained is 9.16 eV.

According to Fig. 2, the GGA energy profile without Hubbard $U$ correction is represented by a convex parabola, and in the next section, we will show that this convex parabola behavior will introduce some absurd results by the so-called delocalization error [22], while more reasonable results will be obtained in GGA + $U$ and HDFT methods with proper parameters, whose energy functional satisfies the general Koopmans' condition to eliminate the delocalization error. Any $U$ value in the range of 4–5 eV will produce a nearly linear variation of the total energy whose residual errors are smaller than 0.1 eV when $q \in (0, 1)$. This is consistent with the previous semiempirical choice of $U$ for Ti ion in $Al_2O_3$ and a variety of other materials [30,33–37]. Both PBE0 and HSE06, two popular HDFT methods, approximately satisfy the general Koopmans' condition that their residual errors are also smaller than 0.1 eV.

Furthermore, we find that GGA + $U$ produces a similar approximate energy function as HSE06 and PBE0 do when the value of $U$ is between 4 and 5 eV. The behaviors of $U = 4$ eV function and HSE06 are very close, so are for $U = 5$ eV function and PBE0, in that their difference for each group is smaller than 0.05 eV. The more accurate $U$ value could be obtained by subdividing the interval ranging from 4 to 5 eV, but considering the uncertainties brought about by the difference in charge corrections and equilibrium geometries needed for different functionals, we choose $U = 4$ eV based on the fact that its energy function behavior is close to HSE06 as an approximation [37].

### C. The binding energy of Ti pairs

We construct a pair of Ti ions by replacing two nearest- or next-nearest-neighboring Al ions in a given supercell, which are termed *nearest* and *next* configurations, respectively. Then the GGA method with and without Hubbard $U$ correction is applied to relax these two configurations to get their optimized structures. To obtain the binding energies of nearest and next configurations in the isolated limit, the extrapolation method

has been used for GGA and GGA + $U$ results, respectively, and Table II lists the binding energy after correction. In addition, our extrapolation results find that the Hubbard $U$ method has little impact on the image-charge correction. To compare with the result in the Hubbard $U$ correction, the hybrid functionals illustrated in Fig. 2 are also adopted to calculate the binding energy of Ti pairs, and results are also listed in Table II. Owing to the computational demand of the HDFT method, only the 120-atom supercell is employed. The correction required to obtain the isolated limit comes from the extrapolation result of the GGA + $U$ method by assuming the similarity of corrections in different methods.

As listed in Table II, significant binding tendencies in $Ti^{3+}$-$Ti^{3+}$ and $Ti^{3+}$-$Ti^{4+}$ pairs turn up in the GGA method, which fails to describe the localization effect of the $3d$ electron correctly. In comparison, GGA + $U$, PBE0, and HSE06 give similar and much weaker binding tendencies of $Ti^{3+}$-$Ti^{3+}$ and $Ti^{3+}$-$Ti^{4+}$ pairs than the GGA method does. This result suggests that the strong binding tendencies of $Ti^{3+}$-$Ti^{3+}$ and $Ti^{3+}$-$Ti^{4+}$ pairs in the GGA method should be artificial and overestimated according to their different energy function behaviors in Fig. 2 [22]. In addition, it is found that the binding tendency of $Ti^{3+}$-$Ti^{3+}$ and $Ti^{3+}$-$Ti^{4+}$ pairs decreases when $\alpha$ is increasing in the HSE functional, which consists of the energy function behavior in Fig. 2 that concave functionals will punish the delocalization tendency. As for $Ti^{4+}$-$Ti^{4+}$ pairs, all methods produce similar results as a consequence of lacking $3d$ electrons in Ti pairs, which is similar to a $TiO_2$ case that a small value of $U = 0.15$ eV was derived by a different procedure [72].

Further evidence for delocalization errors in GGA results is the unreasonable binding energy of Ti pairs in *remote* configuration, which is constructed by replacing two farthest Al ions in the 960-atom supercell with Ti ions, i.e., one site is at the center and another site is at the corner of the supercell. Table III lists the binding energy of the Ti pair in *remote* configuration in the GGA and GGA + $U$ methods. The distance of these two Ti's is more than 17 Å, but in the GGA method, the binding energy of $Ti^{3+}$-$Ti^{4+}$ is still considerable, while with the Hubbard $U$ correction, the artificial binding energy disappears.

This anomaly of $Ti^{3+}$-$Ti^{4+}$ binding energy in the remote configuration provides an intuitive glance for the intrinsic drawback of the general GGA method: Owing to minimizing the total energy of Ti ions, a $3d$ electron is preferred to equally distribute evenly on two Ti ions to reduce the total energy, even though they are far apart. This has been shown by the convexity of the $U = 0$ curve in Fig. 2. If we employed two artificial $Ti_{Al}^{0.5+}$ defects as a reference, rather than a $Ti^{3+}$ defect and a $Ti^{4+}$ defect in Eq. (3), the binding energy of the actual $Ti^{3.5+}$-$Ti^{3.5+}$ in the remote configuration was very close to 0.00 eV. This interesting result indicates that the erroneous delocalization effect for a Ti $d$ electron in GGA drives a more preferred electronic configuration as $Ti^{3.5+}$-$Ti^{3.5+}$ for a $Ti^{3+}$-$Ti^{4+}$ pair in the GGA method. More details about the structure of $Ti^{3+}$-$Ti^{4+}$ pair will be discussed in Sec. III D.

Meanwhile, we notice that the binding energies of these Ti pairs in the remote configuration deviate slightly from 0.00 eV in the GGA + $U$ method. This might be caused by the

TABLE II. The binding energies of Ti pairs in isolated limit (units: eV).

| Configuration | $Ti^{3+}$-$Ti^{3+}$ | | $Ti^{3+}$-$Ti^{4+}$ | | $Ti^{4+}$-$Ti^{4+}$ | |
| Method | Nearest | Next | Nearest | Next | Nearest | Next |
|---|---|---|---|---|---|---|
| GGA | −0.90 | −0.98 | −0.74 | −0.80 | 0.28 | 0.20 |
| GGA + $U$ | −0.12 | −0.07 | −0.05 | −0.07 | 0.35 | 0.34 |
| PBE0 | −0.08 | −0.15 | −0.10 | −0.18 | 0.30 | 0.31 |
| HSE06 | −0.12 | −0.15 | −0.19 | −0.25 | 0.28 | 0.29 |
| HSE(0.40, 0.2) | −0.06 | −0.08 | 0.03 | −0.06 | 0.30 | 0.30 |
| HSE(0.60, 0.2) | −0.02 | −0.04 | 0.07 | 0.06 | 0.31 | 0.30 |

systematic error in our image-charge correction for Ti pairs in the remote configuration. We suppose that the distance of two Ti ions is far enough, the interaction between these two Ti ions can be ignored, and the extrapolation result for $Ti^{4+}$ ion is directly adopted for the image-charge correction of charged Ti pairs in remote configuration. Moreover, we neglect the defect-induced elastic energy in the 960-atom supercell as such a term is expected to decay fast with increasing supercell size.

To further illustrate the delocalization error in the GGA method, we use the GGA method to calculate the binding energies of Ti pairs at the optimized geometric structures obtained by GGA + $U$ and HSE06 in the 120-atom supercell and, as a comparison, similar calculations are also carried out with GGA + $U$ and HDFT methods. It is found that the GGA method always predicts more stable $Ti^{3+}$-$Ti^{3+}$ and $Ti^{3+}$-$Ti^{4+}$ pairs by about or more than 0.5 eV relative to the GGA + $U$ or HDFT method for the same structures, while the results of GGA + $U$ and HDFT methods are quite similar to each other (see Table S3 in Supplemental Material Sec. S4 [43] for detailed data). This result indicates that the abnormal binding energy for $Ti^{3+}$-$Ti^{3+}$ and $Ti^{3+}$-$Ti^{4+}$ pairs predicted by the GGA method should not be blamed for the inappropriate geometric structures of the pairs, but more relates to the intrinsic problem of the GGA density functional, which fails to describe the localized $3d$ electron properly and introduces the delocalization error.

To sum up, with the localization effect taken into account, such as GGA + $U$ or HDFT, the binding tendencies of $Ti^{3+}$-$Ti^{3+}$ and $Ti^{3+}$-$Ti^{4+}$ pairs are both weak. Taking the two values $E_b = -0.12$ and $-0.25$ eV in Table II and $T = 2000$ K, for example, the aggregation factor $\exp(-E_b/kT) = 2.0$ and 4.3, respectively. This means that for $c_{Ti^{3+}}$ and $c_{Ti^{4+}}$, about 1000 ppm of total aluminium sites, the concentration of the nearest and next-nearest pairs is at the ppm level of the total aluminium site. This is consistent with experiments that $Ti:Al_2O_3$ is a good laser material, while a very high aggregation tendency of the luminescence center would have deteriorated the performance of the laser crystal greatly.

TABLE III. The binding energies of Ti pairs for remote configuration in 960-atom supercell (units: eV).

| Ti pairs | $Ti^{3+}$-$Ti^{3+}$ | $Ti^{3+}$-$Ti^{4+}$ | $Ti^{4+}$-$Ti^{4+}$ |
|---|---|---|---|
| GGA | −0.08 | −0.40 | −0.04 |
| GGA+$U$ | 0.07 | 0.08 | 0.02 |

### D. The geometric structures of $Ti^{3+}$-$Ti^{4+}$ pairs

The optimized nearest configuration of $Ti^{3+}$-$Ti^{4+}$ pair and the corresponding density distribution of the $3d$-electron wave function in the 120-atom supercell by GGA and GGA + $U$ methods are illustrated in Fig. 3. Without the Hubbard $U$ correction, two Ti ions of $Ti^{3+}$-$Ti^{4+}$ pair have nearly the same surrounding environment that actually the pair is like $Ti^{3.5+}$-$Ti^{3.5+}$ configuration by judging from both the structure [Fig. 3(a)] and the charge density distribution of the $3d$ electron [Fig. 3(d)]. However, in GGA + $U$ method, it is obviously that the $3d$ electron tends to localize at one Ti ion to form $Ti^{3+}$ [Figs. 3(b) and 3(e)].

Which $Ti^{3+}$-$Ti^{4+}$ or $Ti^{3.5+}$-$Ti^{3.5+}$ configuration is predicted to be the ground state depends on the parameter settings. Our calculation shows that the $3d$ electron prefers to localize on one Ti ion to form $Ti^{3+}$-$Ti^{4+}$ at least for $3 \leqslant U \leqslant 5$ eV, while in HSE calculations, there is a transition for the ground state from a $Ti^{3.5+}$-$Ti^{3.5+}$ to $Ti^{3+}$-$Ti^{4+}$ configuration that the $3d$ electron prefers to localize on one Ti ion as $\alpha$ in the HSE method increases. In HSE06, the geometry and electronic structure are similar to the GGA result, while for HSE(0.40, 0.2), which produces a more reasonable band gap, the geometry and electronic structures are similar to GGA + $U$ ($U = 4$ eV) result [Figs. 3(c) and 3(f)]. It is noticeable from Figs. 3(e)–3(f) that DFT + $U$ and HSE(0.40,0.2) density functionals make the orbitals of $3d$ more localized than that of GGA in Fig. 3(d). In addition, Bader charge analyses [73] shows that GGA predicts a stronger hybridization between $3d$
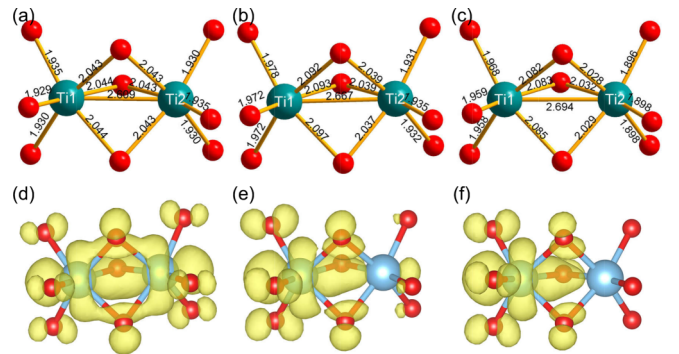


FIG. 3. The optimized nearest configurations of $Ti^{3+}$-$Ti^{4+}$ pair using the GGA (a), GGA + $U$ (b), and HSE(0.40, 0.2) (c) methods. Their corresponding density distribution of $3d$-electron wave functions are plotted in (d)–(f). The average Ti1-O and Ti2-O length in (a) are both 1.987 Å, while in (b) are 2.034 and 1.986 Å, and in (c) are 2.023 and 1.964 Å, respectively.

state of $Ti^{3+}$ and O states than $GGA + U$ and HDFT results (see Supplemental Material Sec. S5 [43] for detailed data).

As for the PBE0 method, which predicts a band gap similar to HSE(0.40, 0.2), the geometry and electronic structures are still similar to the GGA result. However, we also find that the optimized next configuration in PBE0 is very sensitive to the initial structure that actually $Ti^{3+}$-$Ti^{4+}$ configuration is a local minimum with energy only 14 meV higher than the stable $Ti^{3.5+}$-$Ti^{3.5+}$ configuration. To show the delocalization nature of the GGA functional relative to both $GGA + U$ and HSE(0.40,0.2), we have applied GGA and HSE(0.40,0.20) calculations on the fixed geometry structure obtained by $GGA + U$ [Fig. 3(b)], and the obtained charge distributions show no remarkable difference from Figs. 3(d) and 3(f), respectively.

Furthermore, our calculation shows that the difference between the binding energy for $Ti^{3.5+}$-$Ti^{3.5+}$ (obtained from HSE06) and that for $Ti^{3+}$-$Ti^{4+}$ (obtained from $GGA + U$) configurations is always smaller than 0.1 eV when the selected DFT method approximately satisfies Koopmans' condition (see Table S3 in Supplemental Material Sec. S4 [43] for detailed data). We also plot the total energy curve along $Ti^{3+}$-$Ti^{4+}$ and $Ti^{4+}$-$Ti^{3+}$ geometric configurations, and the result shows that the total energy difference between the equal weighted configuration, $Ti^{3.5+}$-$Ti^{3.5+}$, and $Ti^{3+}$-$Ti^{4+}$ is less than 0.05 eV in $GGA + U$ method (see Supplemental Material Sec. S6 [43] for the detailed electronic potential curve). This illustrates the flatness of the total energy surface as the geometric structure and electron configuration switch between $Ti^{3+}$-$Ti^{4+}$ and $Ti^{3.5+}$-$Ti^{3.5+}$.

Whether $Ti^{3.5+}$-$Ti^{3.5+}$ or $Ti^{3+}$-$Ti^{4+}$ should definitely be the ground configuration might be beyond the DFT method adopted here, and additional experiments or more accurate calculation methods such like quantum Monte Carlo method may help. Actually, as an analogy, research on $Ti_4O_7$ materials suggests that there is a complex behavior for the $Ti^{3+}$-$Ti^{4+}$ pair because of strong electronic correlations: the $Ti^{3+}$-$Ti^{4+}$ configuration is more favorable in low temperature, whose total energy also differs from that of $Ti^{3.5+}$-$Ti^{3.5+}$ by ca. 0.1 eV, very close to our result, and there is a phase transition at 150 K that $Ti^{3.5+}$-$Ti^{3.5+}$ becomes dominant at higher temperature [74,75].

Nevertheless, all our $GGA + U$, HSE06, and PBE0 results show that there is no high binding tendency for $Ti^{3+}$-$Ti^{3+}$ and $Ti^{3+}$-$Ti^{4+}$ pairs, regardless of the latter being $Ti^{3+}$-$Ti^{4+}$ or $Ti^{3.5+}$-$Ti^{3.5+}$-type configurations, while the result by the GGA method suffers from the delocalization error. The flatness of the ground-state energy surface along $Ti^{3.5+}$-$Ti^{3.5+}$ and $Ti^{3+}$-$Ti^{4+}$ configurations means that contributions from both need to be taken into account in studying the residual IR absorption in $Ti:Al_2O_3$ crystals.

### E. Introduction to optical transitions in single Ti dopants and Ti-Ti pairs

Before presenting the calculation results, a schematic is introduced here to recall some knowledge about $3d$ energy levels of Ti ions and to provide a walk-through for optical transitions discussed in the next three sections.
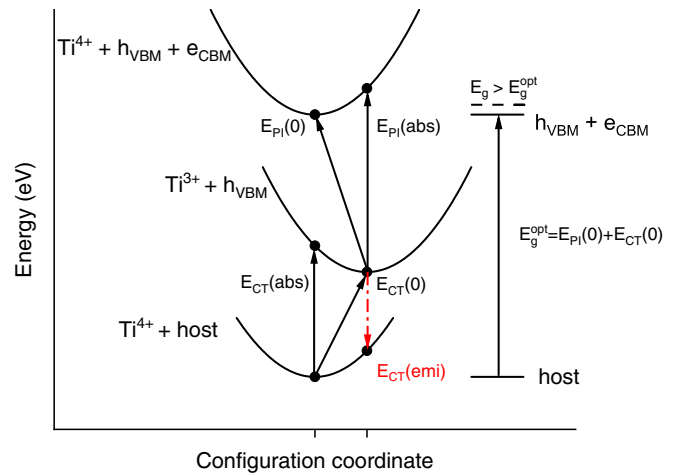


FIG. 4. Schematic configuration coordinate diagram for $Ti^{4+}$ charge transfer and $Ti^{3+}$ photoionization (PI) processes. Here $E_g^{opt}$ and $E_g$ denote, correspondingly, the optical and fundamental band gaps of $Al_2O_3$.

The $3d^1$ orbitals of $Ti^{3+}$ ions in an octahedral crystal field will split to twofold and threefold levels, denoted as $e$ and $t_2$, respectively, and the Jahn-Teller effect makes these levels split further. As for the $Ti^{2+}$ ion, there are two independent sets of energy levels for $3d^2$ electronic configurations, which corresponds to spin parallel and antiparallel situations, and we use their total spins $S = 1$ and $S = 0$ to denote them. More details for these energy levels can be seen in Fig. 6.

Besides these $3d^N$-$3d^N$ transitions for one Ti ions, there are also some transitions which relate to band states of $Al_2O_3$ bulk and trap levels of single Ti dopants in the band gap. We are mainly concerned about $Ti^{4+}$ charge-transfer (CT) transitions and $Ti^{3+}$ photoionizations (PIs). The former transitions correspond to an electron near the VBM being excited and trapped to empty $3d$ orbitals of the $Ti^{4+}$ ion and the latter are excitations from the $3d$ electron of $Ti^{3+}$ to states at or near the conduction band minimum (CBM). Spectra of these transitions in $Ti:Al_2O_3$ have been studied carefully over decades and their features are clear, we therefore apply the DFT scheme to calculate these transitions first in Sec. III F. More details of transition processes are illustrated by the configuration coordinate diagram in Fig. 4. We also apply the calculation scheme in Sec. III F, which is used to obtain transitions between band states of host and trap levels, to calculate the intervalent CT energies in Ti pairs.

Generally, it is difficult to do excited state calculations on top of the DFT method, especially $3d$-$3d$ transitions levels in $Ti^{3+}$-$Ti^{4+}$ and $Ti^{3+}$-$Ti^{3+}$ pairs, which suffer the strong correlation effect of $3d$ electrons. Although the constraint occupancy method can solve these kinds of problems in some cases, this method needs elaborate control to restrict electrons to specific electronic orbits and we have encountered nonconvergence problems in actual calculations. Thus, we combine our DFT method with CAS calculations by using the embedded cluster method presented in Sec. II B.
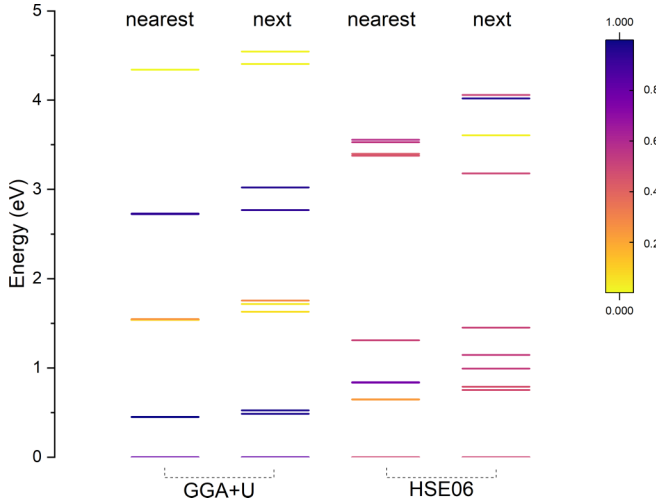
FIG. 5. The $3d^1$ levels obtained with MOLCAS on $Ti^{3+}$-$Ti^{4+}$ structure obtained via the GGA $+ U$ method and $Ti^{3.5+}$-$Ti^{3.5+}$ structure optimized via the HSE06 method, both nearest and next configurations are considered. $Ti_1$–$3d$ and $Ti_2$–$3d$ components dominate all the states shown, and the color of a state is an indication of proportion of the orbital $Ti_1$–$3d$ normalized to total $3d$ components.
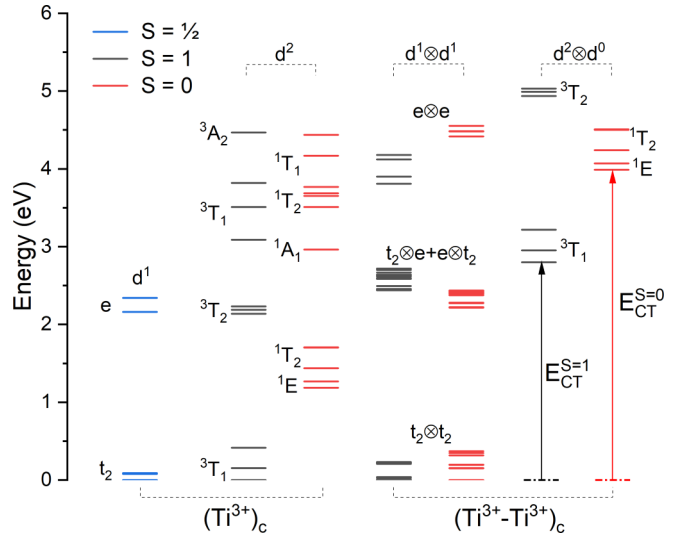


FIG. 6. The energy levels obtained with MOLCAS for different electronic configurations in isolated and the nearest pair of $Ti^{3+}$ equilibrium configurations, which are denoted as $(Ti^{3+})_c$ and $(Ti^{3+}$-$Ti^{3+})_c$, respectively. Energy levels denoted as $d^1$ in the first column belong to $Ti^{3+}$ ions, and the second and third columns are energy levels of $Ti^{2+}$, which is named as $d^2$. The fourth and fifth columns are energy levels of the $Ti^{3+}$-$Ti^{3+}$ pair where two $3d$ electrons are localized on two Ti atoms separately and we denote this situation as $d^1 \otimes d^1$, while levels in the last two columns are also energy levels of the $Ti^{3+}$-$Ti^{3+}$ pair, but two $3d$ electrons are now localized on one Ti ion where actually the electronic structure is $Ti^{2+}$-$Ti^{4+}$ and we denote it as $d^2 \otimes d^0$. The lowest vertical $d^1 \otimes d^1$ to $d^2 \otimes d^0$ spin-allowed transition (CT absorption) is derived as $E_{CT}^{S=1} = 2.80$ eV and $E_{CT}^{S=0} = 4.26$ eV.

As for $Ti^{3+}$-$Ti^{4+}$ pairs, Fig. 5 in Sec. III G shows the hybridization of $3d$ orbitals for two Ti ions in different geometric structures and DFT methods. The $3d$-$3d$ transitions in $Ti^{3+}$-$Ti^{4+}$ pairs is very simple, which just corresponds to $3d$ electron jumps between these $3d$ orbitals.

When it comes to $3d^N$-$3d^N$ transitions in $Ti^{3+}$-$Ti^{3+}$ pairs, the result becomes more complicated. Our calculation shows that there are two different compositions for the energy levels of $Ti^{3+}$-$Ti^{3+}$ pairs as illustrated in Fig. 6. The first kind of energy level corresponds to two $3d$ electrons localized on two $Ti^{3+}$ atoms, respectively (denoted as $d^1 \otimes d^1$), and the transitions from the ground state are similar to $3d$-$3d$ transitions happening in one of the two $Ti^{3+}$'s. If we use $t_2$ and $e$ to denote the $3d$ crystal-field levels, these levels can be divided into three groups $t_2 \otimes t_2$, $t_2 \otimes e + e \otimes t_2$, and $e \otimes e$. The second kind of energy level corresponds to two $3d$ electrons localized dominantly on one Ti ion to form essentially the $Ti^{2+}$-$Ti^{4+}$ (or $Ti^{4+}$-$Ti^{2+}$) electronic configuration, which we denote as $d^2 \otimes d^0$ (or $d^0 \otimes d^2$).

Furthermore, vertical charge-transfer transitions can happen between $d^1 \otimes d^1$ and $d^2 \otimes d^0$ levels that correspond to a $3d$ electron excited from one $Ti^{3+}$ ion to another $Ti^{3+}$ ion to

form a $Ti^{2+}$-$Ti^{4+}$ electronic configuration. However, CASSCF calculations with an embedded cluster meet some problem to obtain an accurate relative position of $Ti^{2+}$-$Ti^{4+}$ to $Ti^{3+}$-$Ti^{3+}$ electronic configuration. An indirect method is proposed by using energy levels of $Ti^{2+}$ and the calculation scheme in Sec. III F to obtain these vertical charge-transfer transitions. More details on obtaining the energy levels of $Ti^{3+}$-$Ti^{3+}$ pairs are referred to in Sec. III H.

Table IV summarizes all the transitions concerned in this paper, which is our assignments to the recent experimental spectra [9] about absorption bands of $Ti:Al_2O_3$ ranging from IR to deep ultraviolet (UV) for a great variety of crystal samples.

TABLE IV. Wavelength ranges and absorption-band peaks in Refs. [9,76] versus calculation results.

| Band label | Measured | | | Calculated | |
| --- | --- | --- | --- | --- | --- |
| | Wavelength range (nm) | Peak wavelength (nm) | Peak energy (eV) | Defects | Peak energy (eV) |
| $Ti^{4+}$ CT | 220–270 | 230 | 5.39 | $Ti^{4+}$ | 5.18 |
| $E$ band | 250–290 | 270 | 4.59 | $Ti^{3+}$-$Ti^{3+}$ | 4.26 |
| Residual UV band | 300–550 | 400 | 3.10 | $Ti^{3+}$-$Ti^{3+}$ | 2.80 |
| Pump band | 400–700 | 490, 550 | 2.53, 2.25 | $Ti^{3+}$ | 2.34, 2.16 |
| IR absorption | 700–1800 | 800 | 1.55 | $Ti^{3+}$-$Ti^{4+}$ | 1.55 |

TABLE V. $Ti^{4+}$ CT and $Ti^{3+}$ PI related energies calculated with the PBE0 type hybrid density functional (energy units: eV).

| | $Ti^{4+}$ CT | | | | $Ti^{3+}$ PI | | |
|---|---|---|---|---|---|---|---|
| | $E_{CT}(0)$ | $E_{CT}(abs)$ | $E_{CT}(emi)$ | Stokes shift | $E_{PI}(0)$ | $E_{PI}(abs)$ | $E_g$ |
| Calc. | 4.27 | 5.18 | 2.94 | 2.24 | 4.89 | 6.23 | 9.16 |
| Expt. [76] | 4.17 | 5.39 | 2.95 | 2.44 | 4.71 | 6.2 [77] | 8.88 |

## F. Transitions between isolated Ti dopants and the host's band states

We first try to calculate energies of $Ti^{4+}$ CT and $Ti^{3+}$ PI, whose corresponding process can be illustrated by using the configuration coordinate model [76] plotted in Fig. 4. The threshold of $Ti^{4+}$ CT, denoted as $E_{CT}(0)$ in Fig. 4, can be represented as

$$E_{CT}(0) = E_{Ti^{3+}}(Ti^{3+}) + h_{VBM} - E_{Ti^{4+}}(Ti^{4+}), \quad (4)$$

Here, the subscript in $E_{Ti^{3+}}(Ti^{3+})$ and $E_{Ti^{4+}}(Ti^{4+})$ means the configuration is fixed at the equilibrium configurations of $Ti^{3+}$ and $Ti^{4+}$, respectively. The energy of the hole, $h_{VBM}$, which is the negative of the energy $e_{VBM}$ as the electron at VBM, can be obtained directly from Kohn-Sham levels in PBE0 calculations from primitive cell by neglecting the influence of doping defects to the band edges of the $Al_2O_3$ bulk in the isolated limit and ignoring the interaction between charged defect center and free hole. All optimized configurations come from our GGA + $U$ results, and we use PBE0 calculations to obtain the total energy difference between $Ti^{4+}$ and $Ti^{3+}$. We also neglected the dependence of the image-charge corrections on DFT method and employed the extrapolation result from the GGA + $U$ method in Eq. (4).

The peak of the $Ti^{4+}$ CT band involves the electronic configuration change while the configuration coordinate is fixed during this transition. As shown by vertical arrows in Fig. 4, $E_{CT}(abs)$ and $E_{CT}(emi)$ are, correspondingly, the peaks of CT absorption and emission bands, which are approximately

$$E_{CT}(abs) = E_{Ti^{4+}}(Ti^{3+}) + h_{VBM} - E_{Ti^{4+}}(Ti^{4+}), \quad (5)$$

$$E_{CT}(emi) = E_{Ti^{3+}}(Ti^{3+}) + h_{VBM} - E_{Ti^{3+}}(Ti^{4+}). \quad (6)$$

As for $Ti^{3+}$ PI, the $3d$ electron is excited from Ti to the conduction band; the threshold and peak energy of the PI band are $E_{PI}(0)$ and $E_{PI}(abs)$, respectively, and we have approximately

$$E_{PI}(0) = E_{Ti^{4+}}(Ti^{4+}) + e_{CBM} - E_{Ti^{3+}}(Ti^{3+}), \quad (7)$$

$$E_{PI}(abs) = E_{Ti^{3+}}(Ti^{4+}) + e_{CBM} - E_{Ti^{3+}}(Ti^{3+}). \quad (8)$$

Here, $e_{CBM}$ denotes the energy of the electron at CBM and the interaction between the conduction-band electron and charged defect center is also neglected.

With the image-charge correction for each defect, we finally list all the CT and PI results in Table V. It is noted that CT and PI results in experiments relates to transitions involving the defect states and various valence-band and conduction-band states of energies different from VBM and CBM, and actually the hole or electron involved does have interaction with charged defect center. Thus, our calculation is just an approximation with at least these two contributions of

opposite signs neglected. Our calculations and experimental results agree reasonably well, indicating the cancellation to a large extent of the two neglected contributions.

In addition, when extrapolation method is adopted to obtain the image-charge correction for $E_{Ti^{3+}}(Ti^{4+})$ and $E_{Ti^{4+}}(Ti^{4+})$, we find that not only the total energies of these charged defects rely on the size of supercell, but also the total energy of neutral defects $Ti^{3+}$ at the equilibrium configuration of $Ti^{4+}$ as $E_{Ti^{4+}}(Ti^{3+})$ needs a size-dependent correction. Interested readers are referred to Supplemental Material Sec. S7 for details [43].

## G. The energy levels and absorption oscillator strengths of $Ti^{3+}$-$Ti^{4+}$ pairs

The absorption due to intervalent CT transition of $Ti^{3+}$-$Ti^{4+}$ has been considered as the culprit of the residual IR absorption in $Ti:Al_2O_3$ crystal [7]. We therefore calculate the $3d^1$ levels of two Ti ions in a $Ti^{3+}$-$Ti^{4+}$ pair according to the CASSCF wave functions and CASPT2 perturbation as mentioned in Sec. II B. Figure 5 shows the energy levels of $Ti^{3+}$-$Ti^{4+}$ pairs and the contribution of a $3d$ orbital for each Ti ion, and Table VI lists these $3d^1$ energy levels of $Ti^{3+}$-$Ti^{4+}$ pairs together with their oscillator strengths. In addition, both HSE06 and GGA + $U$ optimized structures are considered.

As shown in Fig. 5, the hybridization of orbitals from two Ti ions are quite weak for the $Ti^{3+}$-$Ti^{4+}$ structure obtained by the GGA + $U$ method. The low-energy part of the transition levels in $Ti^{3+}$-$Ti^{4+}$ structures can be viewed as an electron jumps from a $3d$ orbital of one Ti ion ($Ti^{3+}$) to the other Ti ion ($Ti^{4+}$). Meanwhile, $3d$ orbitals of two Ti ions hybrid strongly in $Ti^{3.5+}$-$Ti^{3.5+}$ structures obtained from the HSE06 method. This is a natural result because of the similar individual environment for each of the two Ti ions. Figure 5 provides another angle in understanding the $3d$-electron wave functions from VASP in Fig. 3.

The transitions energies of dilute $Ti^{3+}$ ions in $Al_2O_3$ are well characterized in experiment. In Table VI, we compare our calculated results with reported measurements first. $3d - 3d$ excitation energies for $Ti^{3+}$ in our calculation are 2.34 and 2.16 eV, which are not far off from the experimental result [9] of 2.53 and 2.25 eV. The oscillator strength of the main peak in $Ti^{3+}$ is $1.8 \times 10^{-4}$ with local electric field correction. This is consistent with experimental results of $1.4 \times 10^{-4}$ and $3.8 \times 10^{-4}$ in Ref. [9] after considering the sensitivity to local coordination environment for transition metal ions whose forced electric dipole $3d^N$-$3d^N$ transitions are parity forbidden in zeroth order approximation and possible systematic errors in measurements. Moreover, the calculated local-field [57] corrected radiative lifetime of $Ti^{3+}$ is 4.05 $\mu$sec and 4.77 $\mu$sec

TABLE VI. The $3d^1$ levels and electric-dipole oscillator strengths obtained with MOLCAS on $Ti^{3+}$-$Ti^{4+}$ structure obtained via the GGA+$U$ method and $Ti^{3.5+}$-$Ti^{3.5+}$ structure optimized via the HSE06 method, both nearest and next configurations are considered. Only the first six levels for the pairs are included, and for $Ti^{3+}$-$Ti^{4+}$ the first three biased to $Ti_1$ and the next three biased to $Ti_2$. Other excited states are more than 2.7 eV higher than the ground states. The oscillator strength $f$ of the transition from the ground to excited state and $3d^1$ levels of $Ti^{3+}$ are also listed for comparison (energy units: eV).

| Config. Levels | $Ti^{3+}$-$Ti^{4+}$ | | | | $Ti^{3.5+}$-$Ti^{3.5+}$ | | | | Levels | $Ti^{3+}$ | |
|---|---|---|---|---|---|---|---|---|---|---|---|
| | Nearest | $f$ | Next | $f$ | Nearest | $f$ | Next | $f$ | | | $f$ |
| $Ti_1$ $3d_1$ | 0.00 | | 0.00 | | 0.00 | | 0.00 | | $3d_1$ | 0.00 | |
| $Ti_1$ $3d_2$ | 0.45 | $5.5 \times 10^{-6}$ | 0.48 | $1.0 \times 10^{-4}$ | 0.65 | $1.8 \times 10^{-6}$ | 0.75 | $4.1 \times 10^{-4}$ | $3d_2$ | 0.08 | $2.5 \times 10^{-7}$ |
| $Ti_1$ $3d_3$ | 0.45 | $5.5 \times 10^{-6}$ | 0.53 | $8.4 \times 10^{-6}$ | 0.65 | $2.4 \times 10^{-6}$ | 0.79 | $2.4 \times 10^{-4}$ | $3d_3$ | 0.09 | $1.8 \times 10^{-7}$ |
| $Ti_2$ $3d_1$ | 1.54 | $3.3 \times 10^{-4}$ | 1.63 | $7.6 \times 10^{-2}$ | 0.83 | $2.9 \times 10^{-6}$ | 0.99 | $2.9 \times 10^{-5}$ | $3d_4$ | 2.16 | $1.7 \times 10^{-5}$ |
| $Ti_2$ $3d_2$ | 1.54 | $7.3 \times 10^{-4}$ | 1.72 | $3.7 \times 10^{-2}$ | 0.84 | $3.2 \times 10^{-5}$ | 1.15 | $3.0 \times 10^{-6}$ | $3d_5$ | 2.34 | $1.1 \times 10^{-4}$ |
| $Ti_2$ $3d_3$ | 1.55 | $8.4 \times 10^{-2}$ | 1.75 | $2.8 \times 10^{-4}$ | 1.31 | $1.9 \times 10^{-1}$ | 1.45 | $2.2 \times 10^{-1}$ | | | |

for $3d_5$ and $3d_4$ states, similar to 3.87 $\mu$sec measured at low temperature for dilute Ti dopants in $Al_2O_3$ [1].

Based on the oscillator strengths of all those transitions and the expectable large broadening for charge-transfer transitions, the peak of the broad IR absorption band is predicted to be 1.55 eV (800 nm) for nearest and 1.63 eV (760 nm) for next configurations optimized from the GGA + $U$ method, while for HSE06 structures, the energy of the main peak is 1.31 eV (950 nm) for nearest and 1.45 eV (860 nm) for next configurations.

Furthermore, as the ground-state energies of $Ti^{3.5+}$-$Ti^{3.5+}$ and $Ti^{3+}$-$Ti^{4+}$ configurations are very close ($\lesssim 0.1$ eV) and $Ti^{3.5+}$-$Ti^{3.5+}$ and $Ti^{3+}$-$Ti^{4+}$ are just the two limiting cases of the ground-state equilibrium geometry, it can be inferred that the IR absorption will be very broad. This is consistent with the experimental observation that broad IR absorption bands are in the 600–1100 nm wavelength range and centered at ca. 800 nm.

Most importantly, our calculation results of oscillator strengths for $Ti^{3+}$-$Ti^{4+}$ in Table VI are about $10^3$ times larger than that for the pump absorption of $Ti^{3+}$, although part of this large ratio in absorption coefficients will be offset by the larger broadening of the $Ti^{3+}$-$Ti^{4+}$ charge-transfer transition band than the $Ti^{3+}$ $3d$-$3d$ transition band. This result affirmatively shows the importance of eliminating the residual $Ti^{3+}$-$Ti^{4+}$ clusters to an extremely low level in improving the performance of the laser crystals.

### H. The electronic structure of the $Ti^{3+}$-$Ti^{3+}$ pair

Hubbard $U$ correction can also influence the spin of $Ti^{3+}$-$Ti^{3+}$ pairs at ground state, which should be blamed on the correlation error in the GGA method [22]. Without the Hubbard $U$ correction, the spin of the ground state at the nearest configuration is $S = 0$ but is $S = 1$ for the next configuration, and differences between the ground state and their lowest excitation states are 0.17 eV and 0.11 eV, respectively, while the GGA + $U$ method predicts $S = 0$ for both the nearest and next configurations as the ground states, and the lowest $S = 1$ states are no more than 0.05 eV above their $S = 0$ ground states. The various HDFT methods produce similar results as those of GGA + $U$.

Based on embedded cluster calculations, we use CASSCF method with CASPT2 correction to obtain the energy levels of $Ti^{3+}$-$Ti^{3+}$ in nearest configuration (Fig. 6). As the introduction mentioned in Sec. III E, the $Ti^{3+}$-$Ti^{3+}$ pair has two kinds of occupation for two $3d$ electrons on orbitals, $d^1 \otimes d^1$ and $d^2 \otimes d^0$ (or $d^0 \otimes d^2$), which corresponds to two $3d$ electrons localized on two Ti ions, respectively, and both of them localized on one Ti ion.

The energy levels of $d^1 \otimes d^1$ can be divided into three groups $t_2 \otimes t_2$, $t_2 \otimes e + e \otimes t_2$, and $e \otimes e$ as illustrated in Fig. 6. We find that the ground state belongs to $t_2 \otimes t_2$ states in both the nearest and next configurations, and the split of levels in $t_2 \otimes t_2$ is less than 0.4 eV. The middle levels in $d^1 \otimes d^1$ are $t_2 \otimes e + e \otimes t_2$ and the excitation from ground state to the lowest level of $t_2 \otimes e + e \otimes t_2$ is 2.22 eV, and the top levels in $d^1 \otimes d^1$ are $e \otimes e$ states.

It is difficult to obtain accurately the high energy levels of the $d^2 \otimes d^0 + d^0 \otimes d^2$ configuration in CASSCF calculation for an embedded cluster of very limited size for the center part. However, thanks to the empty $3d$-shell of $Ti^{4+}$, the energy level structure of $Ti^{2+}$-$Ti^{4+}$ electronic configuration should be similar to that of an isolated $Ti^{2+}$ ($Ti^{3+}$ at its equilibrium configuration captures an additional electron to become $Ti^{2+}$ electron configuration). Thus, we constructed the energy levels of $Ti^{2+}$-$Ti^{4+}$ electronic configuration direct from that of $Ti^{2+}$ at $Ti^{3+}$ equilibrium configuration in Fig. 6, with the relative position of the lowest $d^2 \otimes d^0$ states relative to the $t_2 \otimes t_2$ ground states, i.e., the vertical CT energy from $Ti^{3+}$-$Ti^{3+}$ to $Ti^{2+}$-$Ti^{4+}$ (denoted as $d^1 \otimes d^1 \to d^2 \otimes d^0$), being estimated by two separate CT processes which we will discuss shortly after.

First, the ground state of $Ti^{2+}$ in Fig. 6 is the spin triplet $^3T_1$, while its excited state is spin singlet $^1T_2 + ^1E$ [78]. The energy difference between the ground state of $^3T_1$ and the average of $^1T_2 + ^1E$ is 1.46 eV by our calculation. As a comparison, the singlet-triplet splitting of $3d^2$ configuration of $V^{3+}$ in $\alpha$-$Al_2O_3$ is 1.2 eV [79]. Our result should be a little bit larger than the case of $Ti^{2+}$ at its own equilibrium configuration, which can be attributed to the shorter surrounding Ti-O distances for the $Ti^{3+}$ equilibrium configuration than those for $Ti^{2+}$.

Then the vertical $d^1 \otimes d^1 \to d^2 \otimes d^0$ charge-transfer transition is equivalent to one $Ti^{3+}$ being excited to $Ti^{2+}$ plus a hole in the valence band followed by the other $Ti^{3+}$ capturing the hole in VBM to become $Ti^{4+}$. If the extra Coulomb attractive interaction in the $Ti^{2+}$-$Ti^{4+}$ pair is included, the vertical

CT energy can finally be written as

$$
\begin{aligned}
E_{\text{CT}} = {} & E_{\text{Ti}^{3+}}(\text{Ti}^{3+} \rightarrow \text{Ti}^{2+} + h) \\
& + E_{\text{Ti}^{3+}}(\text{Ti}^{3+} + h \rightarrow \text{Ti}^{4+}) \\
& + E_{\text{Coul}}(\text{Ti}^{2+}\text{-Ti}^{4+}),
\end{aligned}
\tag{9}
$$

where the subscript $\text{Ti}^{3+}$ denotes the fixed geometry configuration during the vertical charge-transfer transition. Furthermore, as illustrated in Fig. 6, the total spin of $\text{Ti}^{2+}$ can be $S = 0$ and $S = 1$, where there are two different vertical CT type transitions from $\text{Ti}^{3+}\text{-Ti}^{3+}$ to $\text{Ti}^{2+}\text{-Ti}^{4+}$.

According to our approximation in Sec. III F, $E_{\text{Ti}^{3+}}(\text{Ti}^{3+} \rightarrow \text{Ti}^{2+} + h)$ and $E_{\text{Ti}^{3+}}(\text{Ti}^{3+} + h \rightarrow \text{Ti}^{4+})$ can be written as equations about total energies of isolated Ti ions and Kohn-Sham energies of a free hole. Thus, $E_{\text{Ti}^{3+}}(\text{Ti}^{3+} \rightarrow \text{Ti}^{2+} + h)$ and $E_{\text{Ti}^{3+}}(\text{Ti}^{3+} + h \rightarrow \text{Ti}^{4+})$ can be written as

$$
\begin{aligned}
& E_{\text{Ti}^{3+}}(\text{Ti}^{3+} \rightarrow \text{Ti}^{2+} + h) \\
& = [E_{\text{Ti}^{3+}}(\text{Ti}^{2+}) + h_{\text{VBM}}] - E_{\text{Ti}^{3+}}(\text{Ti}^{3+}), \\
& E_{\text{Ti}^{3+}}(\text{Ti}^{3+} + h \rightarrow \text{Ti}^{4+}) \\
& = E_{\text{Ti}^{3+}}(\text{Ti}^{4+}) - [E_{\text{Ti}^{3+}}(\text{Ti}^{3+}) + h_{\text{VBM}}].
\end{aligned}
\tag{10}
$$

Our VASP results show that for vertical CT between $S = 1$ states, the first two terms in Eq. (9) are 7.46 and $-2.94$ eV. The distance of two Ti ions is 2.70 Å (nearest) and 2.81 Å (next) and the experimentally determined high frequency dielectric constant $\varepsilon_\infty = 3.1$ [80] for $\text{Al}_2\text{O}_3$. Then the Coulomb attractive interaction energy between $\text{Ti}^{2+}$ ($\text{Ti}_{\text{Al}}^{1-}$) and $\text{Ti}^{4+}$ ($\text{Ti}_{\text{Al}}^{1+}$) is estimated at about $-1.72$ eV (nearest) and $-1.65$ eV (next). Thus, the lowest $E_{\text{CT}}^{S=1}$ in Eq. (9) is calculated as 2.80 eV and 2.87 eV for the nearest and next pairs, respectively. In addition, we also use the constraint occupancy method to calculate the energy of $\text{Ti}^{2+}\text{-Ti}^{4+}$ electronic configuration at the $\text{Ti}^{3+}\text{-Ti}^{3+}$ equilibrium configuration and directly obtain $E_{\text{CT}}$, and the result is very close to this estimation.

As for vertical CT happens between $S = 0$ states, according to our calculated lowest $S = 0$ and $S = 1$ levels of $\text{Ti}^{2+}$ at $\text{Ti}^{3+}$ geometry configuration, the lowest $E_{\text{CT}}^{S=0}$ is estimated as 4.2–4.3 eV for the two pairs. Here we have neglected the small difference in energy ($\sim 0.05$ eV) between the lowest $S = 1$ and $S = 0$ states of $\text{Ti}^{3+}\text{-Ti}^{3+}$. These two CT processes in $\text{Ti}^{3+}\text{-Ti}^{3+}$ pairs explain the residual broad UV band around 270 nm (4.6 eV) and $E$ band at 400 nm (3.1 eV) in Ref. [9], both of which have similar square-law dependence on the $\text{Ti}^{3+}$ concentration. The predicted and measured result are consistent with each other reasonably well if we consider several facts: (1) there are several final states for both the triplet and singlet CT transitions scattered in a range of 0.42 eV for $^3\text{T}_1$ and 0.52 eV for $^1\text{T}_2 + ^1\text{E}$, (2) the uncertainty due to the estimation of Coulomb interaction in particular, and (3) the large broadening in measured absorption spectra.

## IV. CONCLUSION

Our first-principles calculation shows that the GGA $+ U$ method ($U = 4$–$5$ eV) can give an approximately linear total energy-charge function similar to HSE06 and PBE0 due to approximately satisfying the generalized Koopmans' condition. In general GGA methods, the total energy function is a convex paraboliclike function of the fractional electron number. It is mainly artificial for the strong binding tendencies of $\text{Ti}^{3+}\text{-Ti}^{3+}$ and $\text{Ti}^{3+}\text{-Ti}^{4+}$ pairs, which are predicted by previous calculations and our PBEsol calculations without the Hubbard $U$ correction, and can be attributed to the delocalization error in general GGA density functionals [22]. More reliable calculations, such as GGA $+ U$ and HDFT methods like PBE0, HSE06, and their modifications, lead to more reasonable results that there is no significant tendency of forming excessive Ti pairs. This is consistent with various experiments, including a recent study [81] on the concentration dependence of the luminescence of $\text{Ti:Al}_2\text{O}_3$, which shows similar spectra for the pump excitation and 600–900 nm emission for a variety of concentrations ranging from 1 to 500 ppm of Ti.

Our calculations show that the equilibrium geometry and electronic structure of $\text{Ti}^{3+}\text{-Ti}^{4+}$ pairs can be $\text{Ti}^{3+}\text{-Ti}^{4+}$-type or $\text{Ti}^{3.5+}\text{-Ti}^{3.5+}$-type configurations, with very small energy differences between them ($\lesssim 0.1$ eV). Both $\text{Ti}^{3+}\text{-Ti}^{4+}$ and $\text{Ti}^{3.5+}\text{-Ti}^{3.5+}$-type configurations can contribute to near-IR absorption in the laser operation wavelength ranges, and the oscillator strengths are three orders of magnitude stronger than the pump absorption of $\text{Ti}^{3+}$. This affirmatively shows the importance of reducing the $\text{Ti}^{3+}\text{-Ti}^{4+}$ complex defects to an extremely low level, i.e., lower in concentration by over three orders of magnitude than $\text{Ti}^{3+}$ dopants in improving the performance of the laser crystals.

As for the $\text{Ti}^{3+}\text{-Ti}^{3+}$ pairs, our calculations illustrate their energy-level diagram of both $d^1 \otimes d^1$ and $d^2 \otimes d^0$ (and similarly, $d^0 \otimes d^2$) electron configurations. Our results show that $\text{Ti}^{3+}\text{-Ti}^{3+}$ pairs do not contribute to the residual IR absorption in the wavelength range of laser operation, but their $d^1 \otimes d^1 \rightarrow d^2 \otimes d^0$ charge-transfer transitions can explain the residual UV band at 270 nm and $E$ band at 400 nm in the absorption spectra of $\text{Ti:Al}_2\text{O}_3$ crystal [9].

In addition, we obtain the energies and Stokes shift of valence-to-$\text{Ti}^{4+}$ charge transfer transitions and ionization energies of $\text{Ti}^{3+}$, which agree with reported experimental results. A particular interesting discovery is revealed in the size-extrapolation process that the image-charge correction is even required for some defects in their neutral charge states at the equilibrium geometry structure of other charge states. This discovery deserves further detailed study for more variety of systems, which may have a significant impact on the prediction of transition energies and Stokes shifts in supercell methods with periodic boundary conditions.

[1] P. F. Moulton, J. Opt. Soc. Am. B **3**, 125 (1986).

[2] A. Sanchez, R. E. Fahey, A. J. Strauss, and R. L. Aggarwal, Opt. Lett. **11**, 363 (1986).

[3] H. Kiriyama, A. S. Pirozhkov, M. Nishiuchi, Y. Fukuda, K. Ogura, A. Sagisaka, Y. Miyasaka, M. Mori, H. Sakaki, N. P. Dover, K. Kondo, J. K. Koga, T. Z. Esirkepov, M. Kando, and K. Kondo, Opt. Lett. **43**, 2595 (2018).

[4] W. Li, Z. Gan, L. Yu, C. Wang, Y. Liu, Z. Guo, L. Xu, M. Xu, Y. Hang, Y. Xu, J. Wang, P. Huang, H. Cao, B. Yao, X. Zhang, L. Chen, Y. Tang, S. Li, X. Liu, S. Li, et al., Opt. Lett. **43**, 5681 (2018).

[5] P. F. Moulton, J. G. Cederberg, K. T. Stevens, G. Foundos, M. Koselja, and J. Preclikova, Opt. Mater. Express **9**, 2131 (2019).

[6] F. Tang, B. Shi, Q. Zhang, C. Zhou, Y. Bu, and J. Li, Laser Phys. **30**, 125802 (2020).

[7] R. L. Aggarwal, A. Sanchez, M. M. Stuppi, R. E. Fahey, A. J. Strauss, W. R. Rapoport, and C. P. Khattak, IEEE J. Quantum Electron. **24**, 1003 (1988).

[8] M. Yamaga, T. Yosida, S. Hara, N. Kodama, and B. Henderson, J. Appl. Phys. **75**, 1111 (1994).

[9] P. F. Moulton, J. G. Cederberg, K. T. Stevens, G. Foundos, M. Koselja, and J. Preclikova, Opt. Mater. Express **9**, 2216 (2019).

[10] W. Kohn and L. J. Sham, Phys. Rev. **140**, A1133 (1965).

[11] C. Lee, W. Yang, and R. G. Parr, Phys. Rev. B **37**, 785 (1988).

[12] A. D. Becke, J. Chem. Phys. **98**, 1372 (1993).

[13] J. P. Perdew, K. Burke, and M. Ernzerhof, Phys. Rev. Lett. **77**, 3865 (1996).

[14] K. Lejaeghere, G. Bihlmayer, T. Björkman, P. Blaha, S. Blügel, V. Blum, D. Caliste, I. E. Castelli, S. J. Clark, A. Dal Corso, S. de Gironcoli, T. Deutsch, J. K. Dewhurst, I. Di Marco, C. Draxl, M. Dułak, O. Eriksson, J. A. Flores-Livas, K. F. Garrity, L. Genovese, et al., Science **351** (2016).

[15] N. Mardirossian and M. Head-Gordon, Mol. Phys. **115**, 2315 (2017).

[16] K. Matsunaga, T. Mizoguchi, A. Nakamura, T. Yamamoto, and Y. Ikuhara, Appl. Phys. Lett. **84**, 4795 (2004).

[17] L. Y. Kravchenko and D. V. Fil, J. Appl. Phys. **123**, 023104 (2018).

[18] L. Y. Kravchenko and D. V. Fil, Phys. Rev. Res. **2**, 023135 (2020).

[19] J. K. Bristow, D. Tiana, S. C. Parker, and A. Walsh, J. Mater. Chem. A **2**, 6198 (2014).

[20] S. Lany and A. Zunger, Phys. Rev. B **80**, 085202 (2009).

[21] P. Deák, Q. Duy Ho, F. Seemann, B. Aradi, M. Lorke, and T. Frauenheim, Phys. Rev. B **95**, 075208 (2017).

[22] A. J. Cohen, P. Mori-Sánchez, and W. Yang, Science **321**, 792 (2008).

[23] G. Kresse and J. Hafner, Phys. Rev. B **47**, 558 (1993).

[24] G. Kresse and J. Hafner, Phys. Rev. B **49**, 14251 (1994).

[25] G. Kresse and J. Furthmüller, Phys. Rev. B **54**, 11169 (1996).

[26] G. Kresse and J. Furthmüller, Comput. Mater. Sci. **6**, 15 (1996).

[27] P. E. Blöchl, Phys. Rev. B **50**, 17953 (1994).

[28] G. Kresse and D. Joubert, Phys. Rev. B **59**, 1758 (1999).

[29] J. P. Perdew, A. Ruzsinszky, G. I. Csonka, O. A. Vydrov, G. E. Scuseria, L. A. Constantin, X. Zhou, and K. Burke, Phys. Rev. Lett. **100**, 136406 (2008).

[30] Y. Hinuma, H. Hayashi, Y. Kumagai, I. Tanaka, and F. Oba, Phys. Rev. B **96**, 094102 (2017).

[31] V. I. Anisimov, J. Zaanen, and O. K. Andersen, Phys. Rev. B **44**, 943 (1991).

[32] S. L. Dudarev, G. A. Botton, S. Y. Savrasov, C. J. Humphreys, and A. P. Sutton, Phys. Rev. B **57**, 1505 (1998).

[33] I. Leonov, A. N. Yaresko, V. N. Antonov, U. Schwingenschlögl, V. Eyert, and V. I. Anisimov, J. Phys.: Condens. Matter **18**, 10955 (2006).

[34] D. D. Cuong, B. Lee, K. M. Choi, H.-S. Ahn, S. Han, and J. Lee, Phys. Rev. Lett. **98**, 115503 (2007).

[35] Z. Hu and H. Metiu, J. Phys. Chem. C **115**, 5841 (2011).

[36] M. Weissmann and R. Weht, Phys. Rev. B **84**, 144419 (2011).

[37] A. C. M. Padilha, J. M. Osorio-Guillén, A. R. Rocha, and G. M. Dalpian, Phys. Rev. B **90**, 035213 (2014).

[38] C. G. Van de Walle and J. Neugebauer, J. Appl. Phys. **95**, 3851 (2004).

[39] C. Freysoldt, B. Grabowski, T. Hickel, J. Neugebauer, G. Kresse, A. Janotti, and C. G. Van de Walle, Rev. Mod. Phys. **86**, 253 (2014).

[40] T. R. Durrant, S. T. Murphy, M. B. Watkins, and A. L. Shluger, J. Chem. Phys. **149**, 024103 (2018).

[41] Y. Kumagai and F. Oba, Phys. Rev. B **89**, 195205 (2014).

[42] C. W. M. Castleton, A. Höglund, and S. Mirbt, Phys. Rev. B **73**, 035215 (2006).

[43] See Supplemental Material at http://link.aps.org/supplemental/ 10.1103/PhysRevB.104.165103 for the details of the extrapolation method in image-charge correction, the check for Gamma integration in different size supercells, the check for structure relaxation of defects in different size supercells, comparison of binding energies of Ti pairs in different DFT methods, Bader charge analyses for $Ti^{3+}$-$Ti^{4+}$ and $Ti^{3+}$-$Ti^{3+}$ pairs, variation of the total energy along the curve from $Ti^{3+}$-$Ti^{4+}$ to $Ti^{3.5+}$-$Ti^{3.5+}$, and a phenomenological model to explain the size-dependent correction for neutral charge defects when doped supercell is highly inhomogeneous, which includes Refs. [[44–50] online].

[44] S. Lany and A. Zunger, Phys. Rev. B **78**, 235104 (2008).

[45] C. Freysoldt, J. Neugebauer, and C. G. Van de Walle, Phys. Rev. Lett. **102**, 016402 (2009).

[46] H.-P. Komsa, T. T. Rantala, and A. Pasquarello, Phys. Rev. B **86**, 045112 (2012).

[47] P. Erhart, B. Sadigh, A. Schleife, and D. Åberg, Phys. Rev. B **91**, 165206 (2015).

[48] C. Varvenne, F. Bruneval, M.-C. Marinica, and E. Clouet, Phys. Rev. B **88**, 134102 (2013).

[49] W. Tang, E. Sanville, and G. Henkelman, J. Phys.: Condens. Matter **21**, 084204 (2009).

[50] G. Makov and M. C. Payne, Phys. Rev. B **51**, 4014 (1995).

[51] F. Aquilante, J. Autschbach, A. Baiardi, S. Battaglia, V. A. Borin, L. F. Chibotaru, I. Conti, L. De Vico, M. Delcey, I. Fdez. Galván, N. Ferré, L. Freitag, M. Garavelli, X. Gong, S. Knecht, E. D. Larsson, R. Lindh, M. Lundberg, P. k. Malmqvist, A. Nenov et al., J. Chem. Phys. **152**, 214117 (2020).

[52] Z. Barandiarán and L. Seijo, J. Chem. Phys. **89**, 5739 (1988).

[53] Z. Barandiarán and L. Seijo, Can. J. Chem. **70**, 409 (1992).

[54] B. O. Roos, P. R. Taylor, and P. E. Sigbahn, Chem. Phys. **48**, 157 (1980).

[55] K. Andersson, P. A. Malmqvist, B. O. Roos, A. J. Sadlej, and K. Wolinski, J. Phys. Chem. **94**, 5483 (1990).

[56] P. Malmqvist, Int. J. Quantum Chem. **30**, 479 (1986).

[57] G. Liu and B. Jacquier, *Spectroscopic Properties of Rare Earths in Optical Materials* (Springer, Heidelberg, 2006).

[58] R. Santos, E. Longhinotti, V. Freire, R. Reimberg, and E. Caetano, Chem. Phys. Lett. **637**, 172 (2015).

[59] W. E. Lee and K. P. D. Lagerlof, J. Electron Microsc. Tech. **2**, 247 (1985).

[60] K. Matsunaga, A. Nakamura, T. Yamamoto, and Y. Ikuhara, Phys. Rev. B **68**, 214102 (2003).

[61] B. Qu, R. Zhou, L. Wang, and P. Dorenbos, J. Mater. Chem. C **7**, 95 (2019).

[62] R. H. French, D. J. Jones, and S. Loughin, J. Am. Ceram. Soc. **77**, 412 (1994).

[63] M. A. Mosquera and A. Wasserman, Mol. Phys. **112**, 2997 (2014).

[64] M. Cococcioni and S. de Gironcoli, Phys. Rev. B **71**, 035105 (2005).

[65] T. Z. H. Gani and H. J. Kulik, J. Chem. Theory Comput. **12**, 5931 (2016).

[66] M. Cococcioni, *Correlated Electrons: From Models to Materials Modeling and Simulation* (Verlag des Forschungszentrum Jülich, Jülich, Germany, 2012).

[67] J. Heyd, G. E. Scuseria, and M. Ernzerhof, J. Chem. Phys. **118**, 8207 (2003).

[68] J. Heyd, G. E. Scuseria, and M. Ernzerhof, J. Chem. Phys. **124**, 219906 (2006).

[69] R. H. French, J. Am. Ceram. Soc. **73**, 477 (1990).

[70] T. Biswas and M. Jain, Phys. Rev. B **99**, 144102 (2019).

[71] F. Viñes, O. Lamiel-García, K. Chul Ko, J. Yong Lee, and F. Illas, J. Comput. Chem. **38**, 781 (2017).

[72] L. A. Agapito, S. Curtarolo, and M. Buongiorno Nardelli, Phys. Rev. X **5**, 011006 (2015).

[73] R. F. Bader, Acc. Chem. Res. **18**, 9 (1985).

[74] S. Lakkis, C. Schlenker, B. K. Chakraverty, R. Buder, and M. Marezio, Phys. Rev. B **14**, 1429 (1976).

[75] X. Zhong, I. Rungger, P. Zapol, and O. Heinonen, Phys. Rev. B **91**, 115143 (2015).

[76] W. C. Wong, D. S. McClure, S. A. Basun, and M. R. Kokta, Phys. Rev. B **51**, 5682 (1995).

[77] V. B. Mikhailik, H. Kraus, D. Wahl, and M. S. Mykhaylyk, Appl. Phys. Lett. **86**, 101909 (2005).

[78] H. H. Tippins, Phys. Rev. B **1**, 126 (1970).

[79] H. U. Rahman and W. A. Runciman, J. Phys. C **4**, 1576 (1971).

[80] D. R. Lide, *CRC Handbook of Chemistry and Physics* (CRC Press, Florida, 2004).

[81] V. B. Mikhailik, P. C. F. Di Stefano, S. Henry, H. Kraus, A. Lynch, V. Tsybulskyi, and M. A. Verdier, J. Appl. Phys. **109**, 053116 (2011).